# USER GUIDE
# Planetary-Code-Collection:
# Thermal and Ice Evolution Models
# for Planetary Surfaces

Norbert Schörghofer (norbert@psi.edu)
Honolulu, Hawaii

2002–2022
Last updated August 5, 2022

# Contents

# Preface

Companion to `https://github.com/nschorgh/Planetary-Code-Collection/`

Cite user guide or source code as:

N. Schörghofer. Planetary-Code-Collection: Thermal and Ice Evolution Models for Planetary Surfaces, 2022. GitHub. doi:10.5281/zenodo.594268 https://github.com/nschorgh/Planetary-Code-Collection/

The most recent release is usually behind the most recent version available on GitHub, but releases have DOIs that can be cited.

Releases are available from GitHub and Zenodo. Each release has a version number and a dedicated DOI, whereas the above DOI refers to all versions, past and future. Individual DOIs are listed at `https://zenodo.org/record/594268`

The Mars Subsurface Ice Model (MSIM) has its own repository and is no longer part of this repository.

# Part 1

# 1D Thermal Model for Planetary Surfaces

1-Dimensional Numerical Model of Thermal Conduction and Surface Energy Balance

The heat flow in the shallow subsurface is described by the heat equation:

$$\rho c \frac{\partial T}{\partial t} = \frac{\partial}{\partial z}\left(k\frac{\partial T}{\partial z}\right) \tag{1.1}$$

where $T$ is temperature, $t$ time, $z$ depth, $\rho c$ the volumetric heat capacity, and $k$ thermal conductivity.

The (negative of the) heat flux is $F = k\dfrac{\partial T}{\partial z}$.

Boundary conditions are specified below.

## 1.1  Semi-Implicit Scheme on Irregular Grid

*Authors & History:* originally implemented by Samar Khatiwala in 2001 (including upper radiation boundary condition for semi-implicit scheme); extended to variable thermal properties and irregular grid by Norbert Schörghofer 2002–2003; added predictor-corrector step in 2019

A flux-conservative discretization on an irregularly-spaced grid is given by

$$\frac{\partial}{\partial z}F_j = \frac{F_{j+\frac{1}{2}} - F_{j-\frac{1}{2}}}{(z_{j+1}-z_{j-1})/2} = 2\frac{k_{j+\frac{1}{2}}\frac{T_{j+1}-T_j}{z_{j+1}-z_j} - k_{j-\frac{1}{2}}\frac{T_j-T_{j-1}}{z_j-z_{j-1}}}{z_{j+1}-z_{j-1}}$$

Subscript $j$ refers to position $z_j$. The spatial discretization of the heat equation (1.1) then becomes

$$
\begin{aligned}
(\rho c)_j \frac{\partial T_j}{\partial t} &= \frac{2k_{j+\frac{1}{2}}}{(z_{j+1}-z_j)(z_{j+1}-z_{j-1})}T_{j+1} - \frac{2}{z_{j+1}-z_{j-1}}\left(\frac{k_{j+\frac{1}{2}}}{z_{j+1}-z_j} + \frac{k_{j-\frac{1}{2}}}{z_j-z_{j-1}}\right)T_j + \\
&\quad + \frac{2k_{j-\frac{1}{2}}}{(z_j-z_{j-1})(z_{j+1}-z_{j-1})}T_{j-1}
\end{aligned}
$$

4

introduce $\quad \alpha_j = \dfrac{\Delta t}{(\rho c)_j} \dfrac{k_{j+\frac{1}{2}}}{(z_{j+1} - z_j)(z_{j+1} - z_{j-1})} \quad$ and $\quad \gamma_j = \dfrac{\Delta t}{(\rho c)_j} \dfrac{k_{j-\frac{1}{2}}}{(z_j - z_{j-1})(z_{j+1} - z_{j-1})}$

$$\frac{\partial T_j}{\partial t} = 2\alpha_j T_{j+1} - 2(\alpha_j + \gamma_j)T_j + 2\gamma_j T_{j-1}$$

(1.2)

A semi-implicit time discretization of (1.1) is of the form (Crank and Nicolson, 1947; Press et al., 1992)

$$(\rho c)_j \frac{T_j^{n+1} - T_j^n}{\Delta t} = \frac{1}{2}\left(\frac{\partial}{\partial z}F_j^{n+1} + \frac{\partial}{\partial z}F_j^n\right)$$

where superscript $n$ refers to the time step. Hence,

$$T_j^{n+1} - T_j^n = \alpha_j T_{j+1}^{n+1} - (\alpha_j + \gamma_j)T_j^{n+1} + \gamma_j T_{j-1}^{n+1} + \alpha_j T_{j+1}^n - (\alpha_j + \gamma_j)T_j^n + \gamma_j T_{j-1}^n$$

which leads to the system of equations

$$\boxed{-\alpha_j T_{j+1}^{n+1} + (1 + \alpha_j + \gamma_j)T_j^{n+1} - \gamma_j T_{j-1}^{n+1} = \alpha_j T_{j+1}^n + (1 - \alpha_j - \gamma_j)T_j^n + \gamma_j T_{j-1}^n} \quad 1 < j < N$$

(1.3)

This tridiagonal linear system can be solved in $O(N)$ steps.

Whereas the temperature $T_j$ is defined on grid point $z_j$, the conductivity $k$ is defined in between points. In the equations above, $(\rho c)_j$ is defined on $z_j$, but in the program implementations, $2(\rho c)_j = (\rho c)_{j+\frac{1}{2}} + (\rho c)_{j-\frac{1}{2}}$. In this way, the thermal properties $k$ and $\rho c$ are defined on the same points. And they do not need to be defined at an interface of two layers with different thermal properties when that interface coincides with a grid point. Since array indices must be integers, we choose $\texttt{k[j]} = k_{j-\frac{1}{2}}$, and the same for $\rho c$.

Although the derivation was made with time-constant thermal parameters $k$ and $\rho c$, it remains valid if these parameters change slowly with time.

### 1.1.1 Upper boundary condition: Stefan-Boltzmann radiation law

The surface energy balance is given by

$$Q + k\left.\frac{\partial T}{\partial z}\right|_{z=0} = \epsilon\sigma T^4\big|_{z=0}$$

(1.4)

$Q$ is the incoming solar flux including any atmospheric contribution. On the right-hand side, $\epsilon$ is the (infrared) emissivity of the surface and $\sigma$ is the Stefan-Boltzmann constant. To apply an implicit method, the nonlinear boundary condition needs to be linearized.

Introduce the auxiliary quantity $T_0$, such that surface temperature $T_s = (T_0 + T_1)/2$

$$\left.\frac{\partial T}{\partial z}\right|_{z=0} = \frac{T_1 - T_0}{\Delta z} \quad \text{and} \quad T^4\big|_{z=0} = \left(\frac{T_0 + T_1}{2}\right)^4 \quad \text{with} \quad \Delta z = 2z_1$$

$T = T_r + T' \qquad T_r$ is a reference temperature around which we linearize

$$\begin{aligned}
Q + k_{1/2}\frac{T_1 - T_0}{\Delta z} &= \epsilon\sigma\left(\frac{2T_r + T_0' + T_1'}{2}\right)^4 \\
&\approx \epsilon\sigma T_r^4 + 2\epsilon\sigma T_r^3(T_0' + T_1') = -3\epsilon\sigma T_r^4 + 2\epsilon\sigma T_r^3(T_0 + T_1)
\end{aligned}$$

$T_0 \left( \frac{k_{1/2}}{\Delta z} + B(T_r) \right) = Q + 3\epsilon\sigma T_r^4 + T_1 \left( \frac{k_{1/2}}{\Delta z} - B(T_r) \right)$ where $B(T_r) = 2\epsilon\sigma T_r^3$.

Introduce $a = (Q + 3\epsilon\sigma T_r^4) / \left( \frac{k}{\Delta z} + B \right)$ and $b = \left( \frac{k_{1/2}}{\Delta z} - B \right) / \left( \frac{k_{1/2}}{\Delta z} + B \right)$.

The relation for $j = 1$ is then

$$-\alpha_1 T_2^{n+1} + (1 + \alpha_1 + \gamma_1 - \gamma_1 b^{n+1}) T_1^{n+1} = \alpha_1 T_2^n + (1 - \alpha_1 - \gamma_1 + \gamma_1 b^n) T_1^n + \gamma_1 (a^n + a^{n+1}) \quad (1.5)$$

Define $\beta = \frac{\Delta t}{(\rho c)_1} \frac{1}{2\Delta z^2}$, then $\alpha_1 = \beta k_{3/2}$ and $\gamma_1 = \beta k_{1/2}$. The surface temperature is computed as

$$T_s = \frac{1}{2}(T_0 + T_1) = \frac{1}{2}(a + bT_1 + T_1)$$

Choose $T_r^n = T_s^n$. The semi-implicit solver with this boundary condition is implemented in `conductionQ.f90`.

The uppermost layer is a half-layer, and the first few grid points must be chosen as $z_0 = 0$ and $z_2 = 3z_1$ (in other words $z_1 = \Delta z/2$, $z_2 = z_1 + \Delta z$). The coefficients for the nonlinear upper boundary condition are designed for that. Subroutine `setgrid` can be used to generate a suitable grid.

*Modified treatment of the upper boundary helpful in some situations:* The linearization of the Stefan-Boltzmann law, $\sigma T^4$, works well as long as the surface temperature changes slowly. The above approximation works very well for most situations, such as Mars orbit and a horizontal surface. A temporary instability, where the surface temperature overshoots significantly, was encountered in two situations: i) A sloped, shadowed surface emerges into sunlight. In this case the energy input changes abruptly. ii) For asteroid orbits with high eccentricity and very small perihelion distances, when the pole emerges from winter into sunlight near perihelion. This transition is continuous, but the change in input energy is nevertheless dramatic.

Above, the thermal emission is linearized around the reference temperature $T_r^n = T_s^n$. If $T_s^{n+1}$ is far from $T_s^n$, a significant error was incurred in the evaluation of the emitted energy. This can be addressed by repeating the calculation with a new reference temperature $T_r$ somewhere in between $T_s^n$ and $T_s^{n+1}$. An empirical choice is the geometric mean between the previous reference temperature and the new surface temperature. This method is essentially a predictor-corrector step, iteratively applied until $T_r$ is within 20% of $T_s^{(n+1)}$.

Another approach is "artificial flux smoothing" where the time step is subdivided into many substeps, using linear interpolation of the incoming flux from $Q^n$ to $Q^{n+1}$. It turns a discontinuous change in $Q$ into a continuous change. However, this approach does not identify a nascent instability or answer how many substeps are required to cure it.

## 1.1.2 Upper boundary condition: prescribed $T$

The general formulas (1.2,1.3) with $T_0 = T_s$ and $z_0 = 0$ yield

$$\alpha_1 = \frac{\Delta t}{(\rho c)_1} \frac{k_{3/2}}{(z_2 - z_1)z_2} \quad \text{and} \quad \gamma_1 = \frac{\Delta t}{(\rho c)_1} \frac{k_{1/2}}{z_1 z_2}$$

The relation for $j = 1$ becomes

$$-\alpha_1 T_2^{n+1} + (1 + \alpha_1 + \gamma_1) T_1^{n+1} = \alpha_1 T_2^n + (1 - \alpha_1 - \gamma_1) T_1^n + \gamma_1 (T_s^n + T_s^{n+1}) \quad (1.6)$$

which is implemented in `conductionT.f90`. This is a standard Crank-Nicolson solver for an irregular spaced grid.

### 1.1.3 Lower boundary condition

(assume $z_{N+1} - z_N = z_N - z_{N-1} =: \Delta z$)
No heat flux: $F_{N+\frac{1}{2}} = 0 \quad \Rightarrow \quad k_{N+\frac{1}{2}}(T_{N+1} - T_N) = 0 \quad \Rightarrow \quad T_{N+1} = T_N$

$$(1 + \gamma_N)T_N^{n+1} - \gamma_N T_{N-1}^{n+1} = (1 - \gamma_N)T_N^n + \gamma_N T_{N-1}^n$$

$$\gamma_N = \frac{\Delta t}{(\rho c)_N} \frac{k_{N-\frac{1}{2}}}{2(z_N - z_{N-1})^2}$$

With geothermal heating: $F_{N+\frac{1}{2}} = F_{\text{geothermal}} \quad \Rightarrow \quad k_{N+\frac{1}{2}}(T_{N+1} - T_N) = \Delta z F_{\text{geothermal}}$

$$(1 + \gamma_N)T_N^{n+1} - \gamma_N T_{N-1}^{n+1} = (1 - \gamma_N)T_N^n + \gamma_N T_{N-1}^n + \frac{\Delta t}{(\rho c)_N} \frac{F_{\text{geothermal}}}{\Delta z} \tag{1.7}$$

### 1.1.4 Validations

The following tests were performed for these solvers:

a) For a sinusoidally varying surface temperature, the solution to the heat equation is known analytically:

$$T = T_m + T_a e^{-z/\delta} \sin\left(\frac{z}{\delta} - \frac{2\pi t}{P}\right) \tag{1.8}$$

where

$$\delta = \frac{\Gamma}{\rho c} \sqrt{\frac{P}{\pi}} \tag{1.9}$$

is the thermal skin depth, $\Gamma$ the thermal inertia, and $P$ the period. This expression can be used to validate `conductionT` for uniform thermal properties (Figure 1.1). The heat flux is given by

$$F = -k\frac{\partial T}{\partial z} = -\sqrt{2}\,k\frac{T_a}{\delta}e^{-z/\delta}\cos\left(\frac{z}{\delta} - \frac{2\pi t}{P} + \frac{\pi}{4}\right)$$

b) Convergence of some solutions with $\Delta t$ and $\Delta z$ has been verified.

c) For periodic solutions (of `conductionT` and `conductionQ`) the heat flux $F = -k\partial T/\partial z$, time-averaged over one period, must be the same at all depths and equal to the heat flux imposed at the bottom boundary, even for spatially-varying thermal properties, as long as the heat capacity does not vary with time; consider the time average of eq. (1.1). Figure 1.2 shows one example.

d) A short-term solution for the heat equation with Stefan-Boltzmann radiation surface boundary condition was derived by Handelsman and Olmstead (1972). Their non-dimensional equations are $T_t = T_{zz}$, $T_z(0,t) = T^n(0,t) - f(t)$, $T(z,0) = 0$, $\lim_{z\to\infty} T(z,t) = 0$. In our case $n = 4$ and $f(t) = T_e^4$, where $T_e$ is an ambient temperature. In this case, their
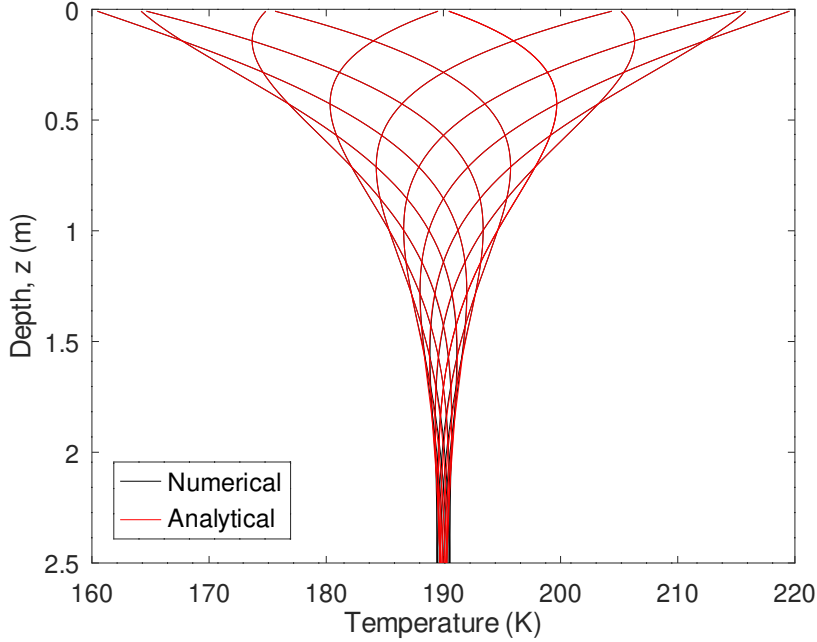
Figure 1.1: Comparison of numerical with analytical solution for Crank-Nicolson solver with periodic surface boundary condition. The deviations at the bottom are justified because the analytical solution (1.8) is for an infinitely deep domain. Non-equidistant grid points were used in this example.

solution is $T(0,t) = \frac{2}{\sqrt{\pi}} T_e^4 \sqrt{t}$, for small $t$. After re-dimensionalizing, the surface temperature is found to change as

$$T(0,t) = T_0 + \frac{2}{\sqrt{\pi}} \frac{\epsilon\sigma}{\Gamma} \left(T_e^4 - T_0^4\right) \sqrt{t} \qquad \text{for small } t \geq 0 \qquad (1.10)$$

where $T_0 = T(0,0)$ is the initial surface temperature. Figure 1.3 shows that the numerical solver reproduces the expected behavior for this discontinuous change in incoming flux.

e) When applied to Mars, modeled surface temperatures have been compared to TES (Thermal Emission Spectrometer) surface temperatures.

Table 1.1: Current implementations of 1D heat equation solvers. `conductionT/Q` are provided in four languages: Fortran, C, Matlab, and Python.

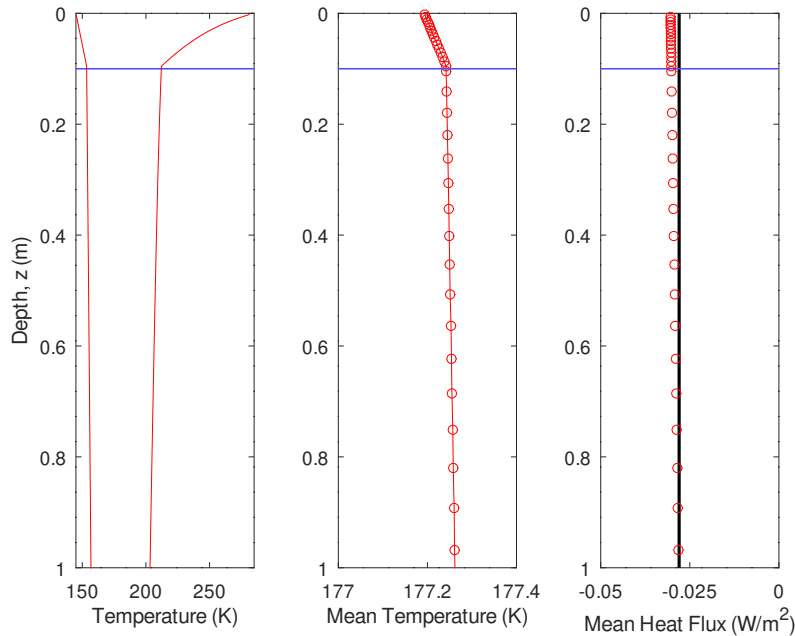| Subroutine | Description |
|---|---|
| `conductionT.f90` | standard Crank-Nicolson solver |
| `conductionQ.f90` | Crank-Nicolson with $\sigma T^4$ emission at upper boundary |
| `conductionT2.f90` | version of `conductionT` that precomputes coefficients |
| `conductionQ2.f90` | version of `conductionQ` that precomputes coefficients |

Figure 1.2: Validation of the conservation of the heat flux (flux-conservative discretization). The ice table at 10 cm depth causes dramatic changes in thermal properties. Left panel: Minimum and maximum subsurface temperatures over one Mars year. Middle panel: Temperatures averaged over one Mars year, which change linearly as the thermal conductivity is constant within each of the two layers. Right panel: Heat flux averaged over one Mars year, which is preserved across changes in thermal properties and equals to the heat flux imposed at the bottom boundary of 0.028 W/m$^2$.

## 1.2 Other Model Components

### 1.2.1 Incidence angle and orbits

The elevation $\beta$ of the sun above an horizontal horizon is given in terms of geographic latitude $\lambda$, declination $\delta$ of the sun, and the hour angle $h$ by

$$\sin \beta = \cos \lambda \cos \delta \cos h + \sin \lambda \sin \delta. \tag{1.11}$$

Table 1.2: Subroutines that provide sun positions.

| Subroutine | Description |
| --- | --- |
| generalorbit.f | general ellipsoidal orbit (solves Kepler's equation with Newton method) |
| marsorbit.f90 | orbit for present-day Mars |
| sunpos.f90 | sun position for Earth |

NASA's SPICE Toolkit provides the sun position for solar system bodies, and can be used instead of the subroutines listed in Table 1.2.
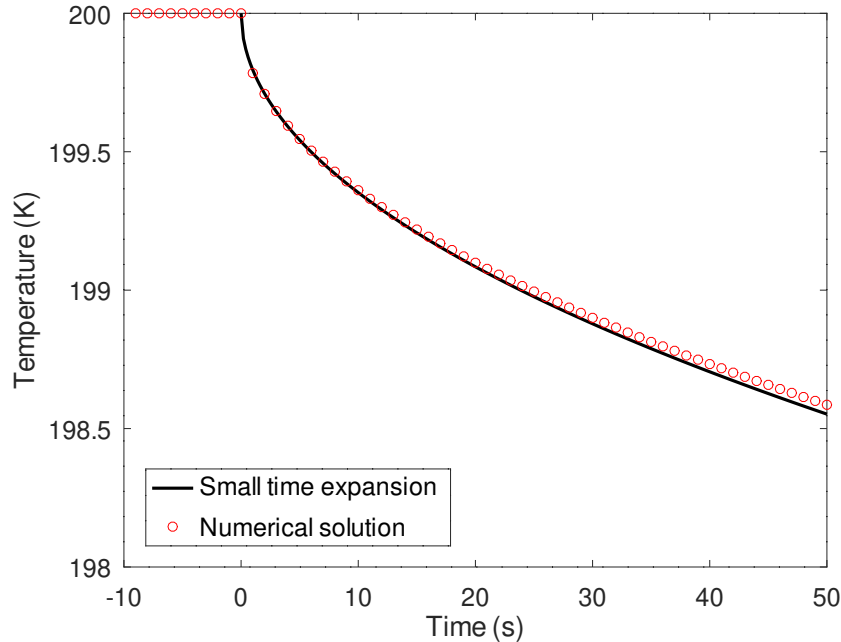
Figure 1.3: Response of numerical solution to a sudden change in incoming flux compared to the analytically obtained expansion for small times, eq. (1.10).

## 1.2.2 Seasonal frost cover

For Mars, the surface energy balance with the latent heat of $CO_2$ sublimation added is

$$Q + k \left.\frac{\partial T}{\partial z}\right|_{z=0} = \epsilon\sigma T^4\big|_{z=0} + L\frac{dm_{CO_2}}{dt} \quad \text{with} \quad m_{CO_2} \geq 0 \tag{1.12}$$

where $L$ is the specific latent heat and $m_{CO_2}$ is the areal density of $CO_2$ ice. See the description in the MSIM repository (`https://github.com/nschorgh/MSIM`) for more details and a program implementation.

## 1.2.3 Thermal properties of the ground

See Winter and Saari (1969) for heat capacity of silicates as a function of temperature. Notably, many silicates have about the same specific heat capacity. See Handbook of Chemistry and Physics (Lide, 2003) for the temperature dependence of ice.

The thermal conductivity varies by four orders of magnitudes on planetary surfaces, primarily due to the dependence on grain size. The parametrization of thermal conductivity in particulate soil is a vast subject. In the terrestrial context, Robertson (1988) provides an extensive compilation of the thermal properties of bulk rock.

Ice can greatly change the thermal properties of porous ground. For example, consult the laboratory measurements by Siegler et al. (2012) for vapor-deposited ice.

In the program, $k$ and $\rho c$ are defined halfway between grid points, whereas $T$ is defined on grid points.

10

### 1.2.4 Thermal model for planar slope

Planar slopes are much simpler than the general 3D problem. This section describes a model for the thermal balance on a tilted plane, in the form of two coupled 1D thermal models.

The elevation $\beta$ of the sun above a horizontal horizon is given by (2.1). The angle $\theta$ of the sun above a sloped surface is

$$\sin\theta = \cos\alpha\sin\beta - \sin\alpha\cos\beta\cos(\Delta a), \tag{1.13}$$

where $\alpha$ is the slope angle and $\Delta a$ is the difference between the azimuth of the sun and the azimuth of the topographic gradient. The sun is assumed to be below the horizon if either $\sin\beta < 0$ (horizontal horizon at infinity) or $\sin\theta < 0$ (self shadowing of slope).

On an airless body the direct insolation is

$$Q_{\text{solar}} = \frac{S_0}{R^2}(1-A)\sin\theta \tag{1.14}$$

where $S_0$ is the solar constant, $R$ the distance from the sun in AU, and $A$ the albedo.

The surface reemits radiation in all directions, but receives additional energy from surfaces in its field of view (terrain irradiance), $Q_{\text{land}}$. This emission is weighted according to the incidence angle $\iota$ (Greek letter iota) and integrated over the spherical angle $\Omega$ subtended by the visible land surfaces. If we consider a horizontal surface at uniform temperature $T_2$ (Kreslavsky and Head, 2005):

$$Q_{\text{land}} = \epsilon_2\sigma T_2^4 \int \cos\iota\, d\Omega = \sin^2\left(\frac{\alpha}{2}\right)\epsilon_2\sigma T_2^4. \tag{1.15}$$

If one assumes $T_2 = T$ and $\epsilon_2 = \epsilon$, then this term can be brought to the right-hand side of eq. (1.4), leading to an effective emissivity of $\epsilon\cos^2(\alpha/2)$. However, this is often not a good approximation, as demonstrated in Aharonson and Schorghofer (2006), Fig. 2b. It is more accurate to base $T_2$ on a separate 1D model for a flat surface.

## 1.3 Semi-Implicit Scheme for Spherically Symmetric Geometry

*History:* developed 2018–2019

Governing equation (1.1) is appropriate for depths small compared to the radius of the body. In the context of small asteroids, it may be necessary to include the curvature effect. A one-dimensional spherically-symmetric semi-implicit heat solver has been implemented (subroutine `conductionT_sphere` in `sphere1d_implicit.f90`). Conceptually, the derivation is the same as in section 1.1. The implementation is limited to constant grid spacing, uniform thermal properties, and a temperature boundary condition on the surface.

The equation for energy conservation in three dimensions is

$$\rho c\frac{\partial T}{\partial t} - \vec{\nabla}\cdot(k\vec{\nabla}T) = 0 \tag{1.16}$$

In the spherically symmetric (1D) case, this equation becomes

$$\rho c \frac{\partial T}{\partial t} = \frac{1}{r^2} \frac{\partial}{\partial r} \left( k\, r^2 \frac{\partial T}{\partial r} \right)$$

For spatially uniform $k$, this simplifies to

$$\frac{\partial T}{\partial t} = \frac{\kappa}{r^2} \frac{\partial}{\partial r} \left( r^2 \frac{\partial T}{\partial r} \right) \tag{1.17}$$

where $\kappa = k/(\rho c)$ is the thermal diffusivity.

The upper (surface) boundary condition is prescribed as a time-dependent temperature $T_0(t)$, which may in turn be obtained from a separate model based on the orbital and physical parameters of the body. At the center of the body $\partial T/\partial r = 0$, which forms the lower boundary condition.

To achieve a spatial discretization that conserves the heat flux, center differences are applied to the equation in the form of (1.17). It would be a mistake to apply the chain rule of differentiation and then discretize. The term in the parenthesis is

$$\left( r^2 \frac{\partial T}{\partial r} \right)_j = r_j^2 \frac{T_{j+1/2} - T_{j-1/2}}{\Delta r}$$

The discretization of the right-hand side of equation (1.17) is:

$$(\text{rhs})_j = \frac{\kappa}{r_j^2 (\Delta r)^2} \left[ r_{j+1/2}^2 T_{j+1} - \left( r_{j+1/2}^2 + r_{j-1/2}^2 \right) T_j + r_{j-1/2}^2 T_{j-1} \right]$$

Introduce $c_{j+1/2} = (r_{j+1/2}/r_j)^2$, $c_{j-1/2} = (r_{j-1/2}/r_j)^2$, and $c_j = (c_{j+1/2} + c_{j-1/2})/2$, then this abbreviates to

$$(\text{rhs})_j = \frac{\kappa}{(\Delta r)^2} \left[ c_{j+1/2} T_{j+1} - 2 c_j T_j + c_{j-1/2} T_{j-1} \right]$$

For an explicit scheme

$$\frac{T_j^{n+1} - T_j^n}{\Delta t} = (\text{rhs})_j^n$$

where the superscripts enumerate time steps. For a semi-implicit (Crank-Nicolson) scheme

$$\frac{T_j^{n+1} - T_j^n}{\Delta t} = \frac{1}{2}(\text{rhs})_j^n + \frac{1}{2}(\text{rhs})_j^{n+1} \tag{1.18}$$

It is useful to introduce the abbreviation

$$\alpha = \kappa \frac{\Delta t}{(\Delta r)^2}$$

For the semi-implicit scheme (1.18),

$$T_j^{n+1} - \frac{\alpha}{2} \left[ c_{j+1/2} T_{j+1}^{n+1} - 2 c_j T_j^{n+1} + c_{j-1/2} T_{j-1}^{n+1} \right] = T_j^n + \frac{\alpha}{2} \left[ c_{j+1/2} T_{j+1}^n - 2 c_j T_j^n + c_{j-1/2} T_{j-1}^n \right]$$

From this results the linear system of equations

$$-\frac{\alpha}{2}c_{j+1/2}T_{j+1}^{n+1} + (1+\alpha c_j)T_j^{n+1} - \frac{\alpha}{2}c_{j-1/2}T_{j-1}^{n+1} = +\frac{\alpha}{2}c_{j+1/2}T_{j+1}^n + (1-\alpha c_j)T_j^n + \frac{\alpha}{2}c_{j-1/2}T_{j-1}^n$$
(1.19)

which is solved numerically by tridiagonal inversion.

At the upper boundary, the temperature $T_0$ is prescribed. For $j = 1$, equation (1.19) becomes

$$-\frac{\alpha}{2}c_{3/2}T_2^{n+1} + (1+\alpha c_1)T_1^{n+1} = +\frac{\alpha}{2}c_{3/2}T_2^n + (1-\alpha c_1)T_1^n + \frac{\alpha}{2}c_{1/2}(T_0^n + T_0^{n+1}) \qquad (1.20)$$

For the lower boundary condition, at the center of the sphere ($j = N$): $\partial T/\partial r = 0$ and therefore $T_{N+1} = T_{N-1}$. Equation (1.19) would then be

$$(1+\alpha c_N)T_N^{n+1} - \alpha c_N T_{N-1}^{n+1} = (1-\alpha c_N)T_N^n + \alpha c_N T_{N-1}^n \qquad (1.21)$$

However, $c_N$ is ill-defined at $r_N = 0$. At the center, $T(r) = T(0) + \beta r^2/2$. Hence, $\partial T/\partial r = \beta r$ and $\partial^2 T/\partial r^2 = \beta$. The divergence of the temperature is

$$\nabla^2 T = \frac{1}{r^2}\frac{\partial}{\partial r}\left(r^2\frac{\partial T}{\partial r}\right) = \frac{2}{r}\frac{\partial T}{\partial r} + \frac{\partial^2 T}{\partial r^2} = \frac{2}{r}\beta r + \beta = 3\beta = 3\frac{\partial^2 T}{\partial r^2}$$

The divergence at the center can thus be evaluated as

$$(\nabla^2 T)_N = 3\frac{T_{N+1} - 2T_N + T_{N-1}}{(\Delta r)^2} = 6\frac{-T_N + T_{N-1}}{(\Delta r)^2}$$

and $(\text{rhs})_N$ is $\kappa$ times this divergence. The lower boundary condition for the semi-implicit scheme becomes

$$(1+3\alpha)T_N^{n+1} - 3\alpha T_{N-1}^{n+1} = (1-3\alpha)T_N^n + 3\alpha T_{N-1}^n \qquad (1.22)$$

In other words, $c_N = 3$, in equation (1.21). For comparison, $c_{N-1} = 5/4$.

# Bibliography

Aharonson, O. and Schorghofer, N., 2006. Subsurface ice on Mars with rough topography. *J. Geophys. Res.* 111(E11):E11007. doi: 10.1029/2005JE002636.

Crank, J. and Nicolson, P., 1947. A practical method for numerical evaluation of solutions of partial differential equations of the heat-conduction type. *Mathematical Proceedings of the Cambridge Philosophical Society* 43(1):50–67.

Handelsman, R. A. and Olmstead, W. E., 1972. Asymptotic solution to a class of nonlinear Volterra integral equations. *SIAM J. Appl. Math.* 22(3):373–384. doi: 10.1137/0122035.

Kreslavsky, M. A. and Head, J. W., 2005. Mars at very low obliquity: atmospheric collapse and the fate of volatiles. *Geophys. Res. Lett.* 32(12):L12202. doi: 10.1029/2005GL022645.

Lide, D. R., editor, 2003. *CRC Handbook of Chemistry and Physics.* CRC Press, 84th edition.

Press, W. H., Teukolsky, S. A., Vetterling, W. T., and Flannery, B. P., 1992. *Numerical Recipes in C*. Cambridge University Press, New York, second edition.

Robertson, E. C., 1988. Thermal properties of rocks. Technical report, US Geological Survey. Open-File Report 88-441, 110pp.

Siegler, M., Aharonson, O., Carey, E., Choukroun, M., Hudson, T., Schorghofer, N., and Xu, S., 2012. Measurements of thermal properties of icy Mars regolith analogs. *J. Geophys. Res.* 117:E03001. doi: 10.1029/2011JE003938.

Winter, D. F. and Saari, J. M., 1969. A particulate thermophysical model of the lunar soil. *Astrophys. J.* 156:1135–1151.

# Part 2

# 3D Surface Energy Balance

Energy Balance with Terrain Shadowing, Terrain Irradiance, and Sky Irradiance

*History:* developed 2010–2019

With 3-dimensional topography the surface energy balance is modified, compared to a horizontal unobstructed planar surface, for the following reasons:

DIRECT IRRADIANCE:
  1) changed incidence angle
  2) elevated horizons (terrain shadowing)

TERRAIN IRRADIANCE:
  3) reflected sunlight from visible land surfaces
  4) infrared emissions from visible land surfaces ("self-heating")

SKY IRRADIANCE (for bodies with atmospheres):
  5) restricted diffuse sky irradiance (short-wavelength and long-wavelength)

The incidence angle on a sloped surface is easily calculated. The elevated horizons change the time of sunset and sunrise, and also reduce the irradiance received from the atmosphere. Horizon determinations require that all other pixels in the domain are considered, and hence represent a non-local computational problem. Sunlight that is reflected from surfaces and the infrared emitted from the same surfaces are known as "terrain irradiance" and computed with the help of "view factors". Calculation of the terrain irradiance is computationally even more demanding than the horizons calculations.

## 2.1   Incidence Angle on Slope; Direct Solar Irradiance

The elevation $\beta$ of the sun above a horizontal horizon is given in terms of geographic latitude $\lambda$, declination of the sun $\delta$, and the hour angle $h$ by

$$\sin \beta = \cos \lambda \cos \delta \cos h + \sin \lambda \sin \delta. \tag{2.1}$$

The angle $\theta$ of the sun above a sloped surface is

$$\sin\theta = \cos\alpha\sin\beta - \sin\alpha\cos\beta\cos(\Delta a), \qquad (2.2)$$

where $\alpha$ is the slope angle and $\Delta a$ is the difference between the azimuth of the sun and the azimuth of the topographic gradient. The sun is assumed to be below the horizon if either $\sin\beta < 0$ (horizontal horizon at infinity) or $\sin\theta < 0$ (self shadowing of slope). For 3D topography, a distant horizon, higher than the self shadowing slope, introduces an additional cutoff $e_{\text{max}}$ (horizon elevation).

On an airless body the direct insolation is

$$Q_{\text{solar}} = \frac{S_0}{R^2}(1 - A)\sin\theta. \qquad (2.3)$$

where $S_0$ is the solar constant, $R$ the distance from the sun in AU, and $A$ the albedo.

## 2.2 Horizons and Multigrids (Terrain Shadowing)

Shadowing by nearby topography (terrain shadowing) defines local horizons and is important for the energy balance. Horizons for each pixel are determined with azimuth rays, typically every 2° in azimuth, and the highest horizon in each direction is stored. For the purpose of horizon determination, the topography is represented by triangular facets. The horizon-finding calculation is implemented in `shadows.f90` and `shadow_subs.f90`.

The topography is defined on a rectangular coordinate grid with spatial resolution $\Delta x$ in the longitude direction and $\Delta y$ in the latitude direction. Curvature effects are not incorporated, i.e., the domain needs to be small compared to the radius of the body. Nor can the domain include the rotational pole. Surface normals are calculated using center-differences in $x$- and $y$-direction, and one-sided differences at the domain boundaries.

*Multigrid Acceleration for Horizons Calculations:* Use of spatial grids with various resolutions (multigrid method) dramatically accelerates the horizons calculation, because cells that are far from the point of interest are larger and fewer (Figure 2.1). For a domain with $N \times N$ pixels, the computational cost without multigrid method is $O(N^4)$. With multigrid, it is $O(N^2 \log N)$. In the current implementation of the multigrid method, up to ten grids can be used; the difference in resolution between the coarsest and finest grids is a factor of $2^{10-1}$. If the multigrid method is not used, an optional cut-off radius `RMAX` can be introduced, so spatial distances larger than `RMAX` are ignored.

First, grids of various resolutions are created, until the coarsest grid consists of only a few pixels along the narrower side of the rectangular domain. Grid coordinates of the coarse cells are also grid coordinates on the finest grid. Progressive downsampling by factors of two involves weighted averaging among the 8 nearest neighbors and the center point itself, such that $\int\int h(x, y)dxdy$ is conserved (other than at the edges of the domain).

The determination of the grid points to be used for each point of interest begins by looping through the coarsest grids. If the distance of the center point to the point of interest is too small, the algorithm proceeds by looping through the four finer cells that make up the coarse cell. This is done recursively, until the resolution is appropriate for the distance or the finest grid is reached. This results in multigrids as in Figure 2.1.
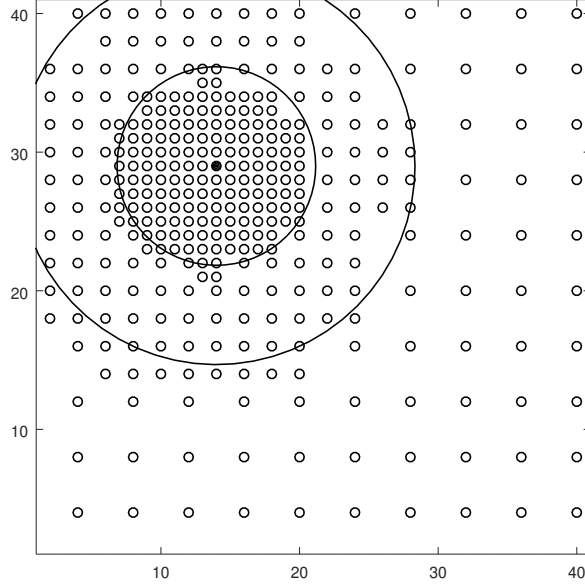
16

Figure 2.1: Example of multigrid (empty dots) used to determine horizons for one point of interest (solid dot). A progressively downsampled topography is used as the distance from the point of interest increases. This example uses three levels of grids.

## 2.3   Governing Equations with Terrain Irradiance

The equation governing the energy balance on the surface on an airless body is

$$(1 - A)(Q_{\text{direct}} + Q_{\text{refl}}) + k\frac{\partial T}{\partial z} + \epsilon Q_{\text{IR}} = \epsilon \sigma T^4 \tag{2.4}$$

where $A$ is albedo, $Q_{\text{direct}}$ incoming solar radiation (insolation), $k$ thermal conductivity, $T$ temperature, $z$ depth below surface, $\epsilon$ emissivity, and $\sigma$ the Stefan-Boltzmann constant. The flux $Q_{\text{direct}}$ is determined from the declination of the Sun, latitude, and hour angle, eqs. (2.1, 2.2). Due to topography, reflected sunlight ($Q_{\text{refl}}$) and thermal emission ($Q_{\text{IR}}$) from other surfaces need to be added.

The diffuse terrain irradiance depends on the spherical angle $d\Omega$ subtended by the facet, and similarly for infrared emission:

$$Q_{\text{refl}}(x, y) = \frac{1}{\pi} \int\int A' \left[Q'_{\text{direct}} + Q'_{\text{refl}}\right] \cos \iota \, d\Omega(x, y, x', y') \tag{2.5}$$

$$Q_{\text{IR}}(x, y) = \frac{1}{\pi} \int\int \left[\epsilon \sigma T'^4 + (1 - \epsilon)Q'_{\text{IR}}\right] \cos \iota \, d\Omega(x, y, x', y') \tag{2.6}$$

where primed variables are evaluated at $(x', y')$ and unprimed variables at $(x, y)$. The integrals are over all facets within the field of view, and $\iota$ is the angle between the surface normal and the line of sight that connects the two facets. The term with the factor $(1 - \epsilon)$ is reflected infrared.

In the literature these equations are often written in terms of a "view factor"

$$V_{ij} = \frac{\cos \iota_i \cos \iota_j}{\pi r_{ij}^2} d\mathcal{A}_j \tag{2.7}$$

17

where $r_{ij}$ is the distance between the two facets, $\iota_i = \iota(x, y)$, $\iota_j = \iota(x', y')$, and $d\mathcal{A}$ the differential surface area. Since

$$d\Omega = \frac{\cos \iota_j}{r_{ij}^2} d\mathcal{A}_j$$

this is equivalent. The discretized equations then take the form

$$Q_{\text{refl}\,i} = \sum_{j'} A_{j'} \left[ Q_{\text{direct}\,j'} + Q_{\text{refl}\,j'} \right] V_{i,j'} \tag{2.8}$$

$$Q_{\text{IR}\,i} = \sum_{j'} \left[ \epsilon \sigma T_{j'}^4 + (1 - \epsilon) Q_{\text{IR},j'} \right] V_{i,j'} \tag{2.9}$$

Equations (2.5) and (2.6) are linear equations for $Q_{\text{refl}}$ and $Q_{\text{IR}}$, widely known as radiosity equations. However, for a time-dependent problem with subsurface heat conduction, it is not necessary to solve the radiosity equations. Instead, these equations can be used as explicit time-stepping procedure with $Q_{\text{refl}}$, $T$, and $Q_{\text{IR}}$ on the right hand side evaluated at the previous time step $n$, whereas $Q_{\text{direct}}$ and $A$ can be evaluated at time step $n + 1$.

## 2.4 View Factors

Mutual visibility is determined by calculating the slope of the line that connects the two surface facets and comparing it to the maximum topographic slope along a ray in the same direction, tracing outward. (Hence there is a sort involved that is not necessary if only horizons are needed.)

Ultimately, the view factor of all mutually visible facets is calculated and stored. For the purpose of view factors, the topography is represented by rectangles. The visibility and view factor calculations are implemented in `fieldofviews.f90` and `fieldofview_subs.f90`.

View factor values can be validated for a bowl-shaped crater (a spherical cap). Inside a sphere of radius $R$

$$\frac{\cos \iota_i \cos \iota_j}{r_{ij}^2} = \frac{\cos^2 \iota}{(2R \cos \iota)^2} = \frac{1}{4R^2} \tag{2.10}$$

for any pair of facets $i, j$. The viewfactor (2.7) is therefore $V_{ij} = d\mathcal{A}_j / (4\pi R^2)$.

The differential solid angle can be written as

$$d\Omega = \cos e \, de \, d\varphi \tag{2.11}$$

where $\varphi$ is azimuth and $e$ the elevation (an angle) above the horizon. The solid angle of the entire landscape within field of view is

$$\Omega_{\text{land}} = \iint d\Omega = \int_0^{2\pi} \int_0^{e(\varphi)} de \, d\varphi \cos e = \int_0^{2\pi} d\varphi \, \sin(e(\varphi)) \tag{2.12}$$

The spherical angle of the visible sky is $\Omega_{\text{sky}} = 2\pi - \Omega_{\text{land}}$. It is also helpful to introduce the abbreviation

$$G = \frac{1}{\pi} \iint \cos \iota \, d\Omega \tag{2.13}$$

For a half-sphere $G = 1$.

Next several special cases, with increasing complexity, are considered:

18

a) In the special case of a surface covered by a dome at uniform temperature,

$$\iint \cos \iota \, d\Omega = \int_0^{2\pi} d\varphi \int_0^{\pi/2} de \sin e \cos e = 2\pi \int_0^{\pi/2} de \sin e \cos e = 2\pi \frac{1}{2} \sin^2(\pi/2) = \pi$$

Hence $G = 1$ and (2.6) becomes $Q_{\mathrm{IR}} = \epsilon \sigma T'^4$ (plus the reflected infrared, but the emissivity of the sky is different from the emissivity of the surface).

b) Planar slope with a single temperature combined with a horizontal surface with another temperature. In this case, $\Omega = 2\alpha$, so that at $\alpha = \pi/2$ a quarter of the sphere remains. For the slope, the horizon height $e(\varphi)$ along direction $\varphi$ is related by $\tan \alpha \cos \varphi = \tan e$.

For integration practice,

$$\begin{aligned}
\iint d\Omega &= \int_{-\pi/2}^{\pi/2} d\varphi \int_0^{e(\varphi)} de \cos e = \int_{-\pi/2}^{\pi/2} d\varphi \sin(e(\varphi)) \\
&= \int_{-\pi/2}^{\pi/2} d\varphi \frac{\tan \alpha \cos \varphi}{\sqrt{1 + \tan^2 \alpha \cos^2 \varphi}} = 2\alpha
\end{aligned}$$

where $\sin e = \tan e / \sqrt{1 + \tan^2 e}$ was used. The integral of interest

$$\begin{aligned}
\iint \cos \iota \, d\Omega &= \int_{-\pi/2}^{\pi/2} d\varphi \int_0^{e(\varphi)} de \sin e \cos e \\
&= \int_{-\pi/2}^{\pi/2} d\varphi \frac{1}{2} \sin^2(e(\varphi)) = \frac{1}{2} \int_{-\pi/2}^{\pi/2} d\varphi \frac{\tan^2 \alpha \cos^2 \varphi}{1 + \tan^2 \alpha \cos^2 \varphi} \\
&= \frac{\pi}{2}(1 - \cos \alpha) = \pi \sin^2 \left(\frac{\alpha}{2}\right)
\end{aligned}$$

In this case, $G = \sin^2(\alpha/2)$ and (2.6) becomes

$$Q_{\mathrm{IR}} = \epsilon \sigma T'^4 \sin^2 \left(\frac{\alpha}{2}\right) \tag{2.14}$$

plus the reflected infrared, which reproduces (1.15).

c) Uniform temperature, locally flat:

$$\iint \cos \iota \, d\Omega = \int_0^{2\pi} \int_0^{e(\varphi)} de \, d\varphi \cos e \sin e = \frac{1}{2} \int_0^{2\pi} d\varphi \sin^2(e(\varphi))$$

$G$ equals $\sin^2 e(\varphi)$ averaged over azimuths. For small $e$, $G \ll \Omega_{\mathrm{land}}/(2\pi)$.

d) Uniform temperature, not locally flat:

$$\sin \theta = \cos \iota = \cos \alpha \sin \beta + \sin \alpha \cos \beta \cos(\Delta a)$$

where $\alpha$ is the local slope angle. There is now also a lower limit on the elevation angle, $e_{\min}(\varphi)$, from the self-shadowing of the slope, so $\sin \theta$ will never become negative, and therefore

$$\tan e_{\min} = -\tan \alpha \cos(\Delta a)$$

19

which can be positive or negative.

The integral of interest is

$$\iint \cos\iota \, d\Omega = \int_0^{2\pi} \int_{e_{\min}(\varphi)}^{e(\varphi)} de \, d\varphi \, \cos e \left[\cos\alpha \sin e + \sin\alpha \cos e \cos(\Delta a)\right] \qquad (2.15)$$

and the integrals over $e$ can be computed as

$$\frac{1}{\pi} \int de \, \cos e \, \sin e = \frac{1}{2\pi} \sin^2 e$$

$$\frac{1}{\pi} \int de \, \cos^2 e = \frac{1}{2\pi}(e + \sin e \cos e)$$

$G$ can be pre-computed from static geometric information:

$$G = \frac{\cos\alpha}{2\pi} \int_0^{2\pi} d\varphi \, (\sin^2 e - \sin^2 e_{\min}) +$$

$$+ \frac{\sin\alpha}{2\pi} \int_0^{2\pi} d\varphi \, \cos(\Delta a)(e + \sin e \cos e - e_{\min} - \sin e_{\min} \cos e_{\min}) \quad (2.16)$$

An approximation for small $e$ is

$$G \approx \frac{\sin\alpha}{\pi} \int_0^{2\pi} d\varphi \, \cos(\Delta a)(\sin e - \sin e_{\min})$$

For comparison, the surface area (in steradian) visible from an inclined surface is

$$\Omega_{\text{land}} = \iint d\Omega = \int_0^{2\pi} \int_{e_{\min}(\varphi)}^{e(\varphi)} de \, d\varphi \, \cos e = \int_0^{2\pi} d\varphi \, (\sin e - \sin e_{\min}) \qquad (2.17)$$

Equations (2.6) and (2.16) invite a particularly useful approximation for the terrain irradiance. Assuming all land within field of view has the same surface temperature, $Q_{\text{IR}}$ can be calculated from $G$ and view factors for individual facets are not required. One choice for the uniform temperature is the (time-dependent) surface temperature of a horizontal and unobstructed surface. Similarly, $Q_{\text{refl}}$ can be calculated the same way when assuming $AQ_{\text{direct}}$ is uniform on land within the field of view. After horizons and $G$ have been calculated, the surface energy balance calculations for each pixel are independent of one another, and the entire model implementation can be easily parallelized.

## 2.5 Diffuse Sky Irradiance in the Presence of Horizons

In the literature more than one definition of (sky) view factor $F_{\text{sky}}$ and various approximations for the sky irradiance are in use; see Flo Heggem et al. (2001) and Rakovec and Zakšek (2012). The geometric factor $F_{\text{sky}}$ defines what fraction of the sky irradiance for an unobstracted location ($F_{\text{sky}} = 1$) still arrives at a location obstructed by terrain.

One option is to assume the energy contribution is proportional to the spherical angle of the visible sky. In this case, $F_{sky}$ is the spherical angle of the visible sky divided by $2\pi$, which can be calculated from either the horizon heights or the sum of view factors of the landscape segments. For a planar slope tilted by an angle $\alpha$, $F_{sky} = 1 - \alpha/2\pi$.

The alternative is to weigh the diffuse irradiance from the atmosphere with the cosine of the incidence angle. This is the view factor $V$ as defined above for land segments. This corresponds to isotropic (Lambertian) radiation from the sky. The factor $F_{sky}$ then becomes identical to $G_{sky}$. For computing the sky view factor, eq. (2.16) can be used with $e_{min}$ replaced by $e$, and $e$ replaced by $\pi/2$:

$$
\begin{aligned}
G_{sky} &= \frac{\cos\alpha}{2\pi} \int_0^{2\pi} d\varphi \, (1 - \sin^2 e) + \frac{\sin\alpha}{2\pi} \int_0^{2\pi} d\varphi \, \cos(\Delta a) \left( \frac{\pi}{2} - e - \sin e \cos e \right) &(2.18) \\
&= \frac{\cos\alpha}{2\pi} \int_0^{2\pi} d\varphi \, \cos^2 e - \frac{\sin\alpha}{2\pi} \int_0^{2\pi} d\varphi \, \cos(\Delta a)(e + \sin e \cos e) &(2.19)
\end{aligned}
$$

This equation can be found in Dozier and Frew (1990). For a planar slope $G_{sky} = \cos^2(\alpha/2)$.

For Mars, in the spirit of the Kieffer approximation (Kieffer et al., 1977),

$$
Q_{a,IR} = \frac{S_0}{R^2} F_{sky} f_{IR} \sin\beta_{noon} \qquad \text{(all day)} \tag{2.20}
$$

and if the sun is up, then

$$
Q_{a,scat} = \frac{S_0}{2R^2}(1 - A) F_{sky} f_{scat} \qquad \text{when } \sin\beta > 0 \tag{2.21}
$$

otherwise $Q_{a,scat} = 0$. See also the description at the MSIM repository `https://github.com/nschorgh/MSIM/`.

For terrestrial applications, other expressions may be available to quantify the sky irradiance. For example, section 3.1 provides a formula for the diffuse short-wave clear-sky irradiance on Mauna Kea. Such formulas for flat unobstracted terrain can be adopted for obstructed topography using a geometric factor $F_{sky}$.

## 2.6   Outline of Implementation

The calculations are separated into two parts.

The first, described in section 2.2, determines the horizons for all pixels and (optionally) view factors of all facets with all other facets. This information is written to files `horizons.dat` and `viewfactors.dat`, respectively. This part is easily parallelized, as calculations for each pixel are independent of one another although the entire topography has to be loaded into memory at once. For parallelization, one slice of the spatial domain is run on each CPU thread. It can be submitted to a computer cluster as an array job.

In the `horizons` file, each line is preceded by the integer pixel coordinates. The file is rectangular, and the number of entries is (number of azimuth rays + 2)×(number of topographic pixels). The `viewfactors` file is giant and it is not rectangular. Each line in the output file corresponds to a topographic pixel and at the beginning specifies the number

of pixels within field of view. Each visible pixel has then three numbers stored with it: The two integer pixel coordinates and the view factor, $V_{ij}$, for this pixel. Non-visible pixels are not stored.

Horizons calculations are implemented in `shadows.f90` and its subroutines. If the view factors are desired, use `fieldofviews.f90`. Horizon heights are also calculated within `fieldofviews.f90`, but with a slightly different algorithm than in `shadows.f90`.

The second part simulates the time evolution of illumination and surface temperature as the sun moves through the sky, using the horizons and (optionally) the field of view as input. The horizons are read in a module called `newhorizons`, which also interpolates horizon elevations for any desired azimuth. The field of view information is read with a separate subroutine. To save memory, the pixel coordinates are stored as 2-byte integers and the view factors as 4-byte floating point numbers, respectively, half of the common byte lengths.

The surface energy balance is integrated over time at steps of a fraction (e.g., 1/50th) of a solar day. Surface temperature and illumination are updated at every time step. The names of the main programs start with `cratersQ_*` (Table 2.1).

Table 2.1: Overview of current implementations

| Main program | Task | Reflections | Parallel |
|---|---|---|---|
| `shadows` | pre-calculate horizons, optional multigrid | N/A | yes |
| `fieldofviews` | pre-calculate view factors, no multigrid | N/A | yes |
| `insol3d_earth` | direct insolation only, Mauna Kea atm. | no | no |
| `insol3d_mars` | direct insolation only, no atmosphere | no | no |
| `cratersQ_equilbr` | equilibrium solution for airless body | yes | no |
| `cratersQ_moon` | airless body | yes | no |
| `cratersQ_mars` | Mars orbit and atmosphere | G-approx. | no |
| `cratersQ_mars_parallel` | Mars orbit and atmosphere | G-approx. | yes |
| `cratersQ_mars_full` | Mars orbit and atmosphere | yes | no |

The current implementations use the following naming convention. The input topography to `horizons.f90` is *name*`.xyz`, and the output will be `horizons.dat` for the sequential implementation or `horizon.`*arg* for the parallel implementation, where *arg* is an integer. `cratersQ_*` expects input files *name*`.xyz`, `horizons.`*name*, and optionally `viewfactors.`*name*. File names and their associated parameters are specified in module `filemanager`, that the user edits.

The model also includes 1D subsurface heat conduction, eq. (1.1). Subsurface temperatures need to be equilibrated, and hence the entire model needs to be run much longer than would be necessary without subsurface heat. Lateral subsurface heat conduction is neglected. Without subsurface conduction, equilibrium temperatures, according to eq. (2.4) with $k = 0$, can be used, and in this case only a few steps of equilibration are needed to account for several orders of reflection.

`insol3d_earth` was used in Schorghofer et al. (2017) and Schorghofer (2018), `cratersQ_mars_parallel` in Schorghofer et al. (2019), `cratersQ_moon` in Hayne et al. (2021), and `cratersQ_mars_full` in Schorghofer (2020).

# Bibliography

Dozier, J. and Frew, J., 1990. Rapid calculation of terrain parameters for radiation modeling from digital elevation data. *IEEE Transactions on Geoscience and Remote Sensing* 28(5): 963–969. doi: 10.1109/36.58986.

Flo Heggem, E. S., Etzelmüller, B., and Berthling, I., 2001. Topographic radiation balance models: sensitivity and application in periglacial geomorphology. *Norsk Geografisk Tidsskrift-Norwegian Journal of Geography* 55(4):203–211. doi: 10.1080/00291950152746531.

Hayne, P. O., Aharonson, O., and Schorghofer, N., 2021. Micro cold traps on the Moon. *Nature Astronomy* 5:169–175. doi: 10.1038/s41550-020-1198-9.

Kieffer, H. H., Martin, T. Z., Peterfreund, A. R., Jakosky, B. M., Miner, E. D., and Palluconi, F. D., 1977. Thermal and albedo mapping of Mars during the Viking primary mission. *J. Geophys. Res.* 82(28):4249–4291. doi: 10.1029/JS082i028p04249.

Rakovec, J. and Zakšek, K., 2012. On the proper analytical expression for the sky-view factor and the diffuse irradiation of a slope for an isotropic sky. *Renewable Energy* 37(1): 440–444. doi: 10.1016/j.renene.2011.06.042.

Schorghofer, N., 2018. Permafrost survey on the Maunakea summit plateau: Final report. Technical report, University of Hawaii. 28pp.

Schorghofer, N., 2020. Mars: Quantitative evaluation of crocus melting behind boulders. *Astrophys. J.* 890:49. doi: 10.3847/1538-4357/ab612f.

Schorghofer, N., Leopold, M., and Yoshikawa, K., 2017. State of high-altitude permafrost on tropical Maunakea volcano, Hawaii. *Permafrost and Periglacial Processes* 28:685–697. doi: 10.1002/ppp.1954.

Schorghofer, N., Levy, J. S., and Goudge, T. A., 2019. High-resolution thermal environment of recurring slope lineae in Palikir Crater, Mars, and its implications for volatiles. *J. Geophys. Res.* 124:2852–2862. doi: 10.1029/2019JE006083.

# Part 3

# Miscellaneous

## 3.1   Mauna Kea Atmosphere

Terrestrial Atmospheric Absorption and Sky Irradiance

*History:* developed around 2013–2016

Sun position as a function of date is based on Blanco-Muriel et al. (2001), translated into Fortran. It provides the zenith angle and azimuth of the sun, and the Earth-sun distance. Implemented in `sunpos.f90`

Clear-sky direct and indirect short-wave irradiance (W/m$^2$) on Mauna Kea, Hawaii Parametrizations in the atmospheric model are mostly based on Nunez (1980), corrected for typos. Implemented in `mk_atmosphere.f90`

$Z$ ... solar zenith angle (radians)
$I_0$ ... clear-sky direct irradiance; $D_0$ ... clear-sky diffuse irradiance
$R$ ... Earth-sun distance in AU
$m, m'$ ... optical air mass (unitless)
$p_0$ ... total pressure (Pa)
$w$ ... precipitable water vapor (cm)
Transmission coefficients:
$\psi_{wa}$ ... water vapor absorption; $\psi_{ws}$ ... water vapor scattering
$\psi_{rs}$ ... Rayleigh scattering
$\psi_{da}$ ... dust absorption; $\psi_{ds}$ ... dust scattering

**Relative air mass:**
simplest approximation: $m = 1/\cos Z$
better approximation (Kasten, 1966):

$$m = \frac{1}{\cos Z + 0.15 \times (93.885 - Z)^{-1.253}} \tag{3.1}$$

if $(m < 0)$, then $m = \infty$
$p_0 = 610$ on Mauna Kea summit

$m' = m \times p_0/1013$

**Water vapor:**
$w = 0.16$ cm for Mauna Kea according to `https://www.gemini.edu/observing/telescopes-and-sites/sites%23MKWV#MKWV` (assuming a typical $\tau(225\text{ GHz})$ of 0.08)

$$\begin{aligned} \psi_{wa} &= 1 - 0.077(w\,m)^{0.30} \quad \text{McDonald (1960)} & (3.2) \\ \psi_{ws} &= 1 - 0.025\,w\,m & (3.3) \end{aligned}$$

**Rayleigh scattering:** 8% at sea level according to Fig 3-3 in Bird and Hulstrom (1981)

$$\psi_{rs} = \exp(-0.08m') \tag{3.4}$$

**Aerosols:** aerosol optical depth on Mauna Kea $= 0.0084 \times (\lambda/1\mu\text{m})^{-1.26}$ (Buton et al., 2013)

$$\begin{aligned} \psi_{ds} &= \exp(-m \times 0.0084 \times 0.5^{-1.26}) & (3.5) \\ \psi_{da} &= \psi_{ds} \quad \text{assumes single scattering albedo of 0.5} & (3.6) \end{aligned}$$

**Direct sunlight:**
$$I_0 = \psi_{wa}\psi_{da}\psi_{ws}\psi_{rs}\psi_{ds} \times (\text{solar constant})/R^2 \tag{3.7}$$
(without the dimensional factors, this is the transmittance)

**Diffuse sunlight:**
$$D_0 = I_0 \cos(Z)\psi_{wa}\psi_{da}\frac{1 - \psi_{ws}\psi_{rs}\psi_{ds}}{2} \tag{3.8}$$
Roundoff issue: if $(D_0 \leq 0)$, then $D_0 = 0$ because of $-0$.

**Total short-wavelength flux:**
$$F = I_0 \cos Z + D_0 \tag{3.9}$$

Roundoff issue: if $(F \leq 0)$, then $F = 0$ because of $-0$.

Not included are the sensible heat flux and long-wave downward radiation.

**Atmospheric contribution with terrain shadowing:** If terrain irradiance is not included in the surface energy balance, it would be a disadvantage to reduce the diffuse sky irradiance due to obstruction by horizons, because that portion of the sky irradiance would need to be replaced by irradiance from land surfaces. If terrain irradiance is included, then see section 2.5 on how to evaluate the sky irradiance.

used in Schorghofer et al. (2017) and Schorghofer (2018)

## 3.2 Asynchronous Model for Temperature, Impact Mixing, and Ice Loss on Asteroids

*History:* developed 2013–2017

Schorghofer (2016) describes this model and applied it to (1) Ceres and (7968) Elst-Pizarro. In brief, it combines diurnally-resolved temperatures, probabilistic impact stirring (only one-dimensional), and the long-term loss of near-surface ice to space due to sublimation and diffusion. It was also used for the ice retreat calculations published in Prettyman et al. (2017). The solar constant gradually increases according to the standard solar evolution model (Gough, 1981). The main program is `asteroid_fast2`.

A significant complexity in this model arises from partially ice-filled pore spaces (necessary to incorporate the consequences of impact stirring), because the re-distribution of ice within the pores due to vapor diffusion and deposition adds another governing equation. This redistribution turned out to be negligible in all cases it was considered. A simpler two-layer version, where pore spaces are either empty or full, is implemented in `asteroid_fast1`, which is very similar to the model described in the supporting information of Sizemore et al. (2017).

Another application of asynchronous coupling is ice loss calculations for asteroids on dynamical orbits, that is, the orbital elements change over time (and continuous-time integration would be too slow). In Schorghofer et al. (2020) this computational method was applied to potentially ice-rich asteroids that originate in the Outer Main Belt.

## 3.3 Lunar Thermal Ice Pump

*History:* 2013 & 2021 lunar thermal ice pump

The concept of downward "pumping" of vapor by periodic temperature cycles, originally developed for Mars, can also be applied to the Moon, as described in Schorghofer and Taylor (2007); Schorghofer and Aharonson (2014); Schorghofer (2022). The governing equations are cast in the form of a boundary value problem, that is, by calculating the mobility of $H_2O$ molecules on the surface and at one specific depth.

One component of these calculations is a model for the surface population of adsorbed water molecules. It involves a stiff differential equation that is solved with a simple implicit method (a backward Euler step). The "bottom point" is the ice table, or, for the purpose of determining whether or not pumping occurs, the depth of minimum sublimation rate, which is estimated by the sublimation rate at time-averaged temperature. Program `oscidea1.f90` is a simple driver program for the ice pump calculations. This model was used in Schorghofer and Aharonson (2014) and Schorghofer and Williams (2020). In the more recent work by Schorghofer (2022), the upper boundary condition has a fixed value instead (`moon_subsdiff_equilbr.f90`).

For the "adsorbate pump", the pumping is too weak for ice sequestration, but the pumping nevertheless causes an increase of adsorbate concentration with depth. Subsurface residence times depend not only on temperature but also on adsorbate density, which requires

nonlinear root-finding.

Instead of a boundary-value formulation, vapor transport is also simulated with a 1D random walk model in `moon_subsdiff_equilbr.f90` that was also used in Schorghofer (2022).

# Bibliography

Bird, R. E. and Hulstrom, R. L., 1981. A simplified clear sky model for direct and diffuse insolation on horizontal surfaces. Technical report, Golden, Colorado. Report No. SERI/TR-642-761.

Blanco-Muriel, M., Alarcón-Padilla, D. C., López-Moratalla, T., and Lara-Coira, M., 2001. Computing the solar vector. *Solar Energy* 70:431–441. doi: 10.1016/S0038-092X(00)00156-0.

Buton, C. et al., 2013. Atmospheric extinction properties above Mauna Kea from the Nearby SuperNova Factory spectro-photometric data set. *Astron. Astrophys.* 549:A8. doi: 10.1051/0004-6361/201219834.

Gough, D. O., 1981. Solar interior structure and luminosity variations. *Solar Physics* 74:21–34. doi: 10.1007/978-94-010-9633-1_4.

Kasten, F., 1966. Albedo and sky radiance measurements in Greenland. *Arch. Meteor. Geophys. Bioklimatol.* B14:206–223. http://hdl.handle.net/11681/5813.

McDonald, J. E., 1960. Direct absorption of solar radiation by atmospheric water vapor. *Journal of Meteorology* 17:319–328. doi: 10.1175/1520-0469(1960)017%3C0319:DAOSRB%3E2.0.CO;2.

Nunez, M., 1980. The calculation of solar and net radiation in mountainous terrain. *Journal of Biogeography* 7:173–186. doi: 10.2307/2844709.

Prettyman, T. H. et al., 2017. Extensive water ice within Ceres' aqueously altered regolith: Evidence from nuclear spectroscopy. *Science* 355:55–59. doi: 10.1126/science.aah6765.

Schorghofer, N., 2016. Predictions of depth-to-ice on asteroids based on an asynchronous model of temperature, impact stirring, and ice loss. *Icarus* 276:88–95. doi: 10.1016/j.icarus.2016.04.037.

Schorghofer, N., 2018. Permafrost survey on the Maunakea summit plateau: Final report. Technical report, University of Hawaii. 28pp.

Schorghofer, N., 2022. Gradual sequestration of water at lunar polar conditions due to temperature cycles. *Astrophys. J. Lett.* 927(2):L34. doi: 10.3847/2041-8213/ac5a48.

Schorghofer, N. and Aharonson, O., 2014. The lunar thermal ice pump. *Astrophys. J.* 788:169. doi: 10.1088/0004-637X/788/2/169.

Schorghofer, N. and Taylor, G. J., 2007. Subsurface migration of H2O at lunar cold traps. *J. Geophys. Res.* 112(E2):E02010. doi: 10.1029/2006JE002779.

Schorghofer, N. and Williams, J.-P., 2020. Mapping of ice storage processes on the Moon with time-dependent temperatures. *Planet. Sci. J.* 1:54. doi: 10.3847/PSJ/abb6ff.

Schorghofer, N., Leopold, M., and Yoshikawa, K., 2017. State of high-altitude permafrost

on tropical Maunakea volcano, Hawaii. *Permafrost and Periglacial Processes* 28:685–697. doi: 10.1002/ppp.1954.

Schorghofer, N., Hsieh, H. H., Novakovic, B., and Walsh, K. J., 2020. Preservation of ice at the polar regions of near-earth asteroids originating in the outer main asteroid belt: A model study with dynamical trajectories. *Icarus* 348:113865. doi: 10.1016/j.icarus.2020.113865.

Sizemore, H. G. et al., 2017. Pitted terrain on dwarf planet Ceres and implications for volatiles. *Geophys. Res. Lett.* 44(13):6570–6578. doi: 10.1002/2017GL073970.

# Part 4

# Surface-bounded Exospheres

Monte-Carlo Model of Ballistically Hopping Molecules in Gravitationally-Bound Exospheres

*History:* developed 2012–2017
Core routines are implemented in `montecarlo.f90`

## 4.1   Introduction

The ballistic trajectories of neutral molecules or atoms in a surface-bounded exosphere are simulated with a Monte-Carlo method. Individual water molecules are launched with probabilistically distributed cartesian velocity components that amount to a random initial azimuth and thermal speed appropriate for the local surface temperature. The model then computes the molecule's impact location and time analytically. An event-driven algorithm is used, where landing and launching events are processed in time-order. Events are scheduled and processed until the molecule is destroyed or lost or until its landing or launch time is beyond the next thermal model time step, when surface temperatures are updated.

Each molecule has a longitude $p_r[1]$, latitude $p_r[2]$, status $p_s$ (on surface $=0$, in-flight $=1$, lost or cold-trapped $< 0$), and time to the next event $p_t$ (until it arrives on the surface or until it will leave the surface). Negative status values can be used to keep track of where the particle is trapped or how it was lost. Surface temperatures are calculated with a 1D thermal model, as in Part 1.

## 4.2   Ballistic Flight on Sphere

$d$ ... flight distance (measured along surface of sphere)
$t$ ... duration of flight
$\tau_{\mathrm{res}}$ ... surface residence time
$\tau_{\mathrm{dissoc}}$ ... photo-destruction time scale
$v_{\mathrm{esc}}$ ... escape speed
$v_1$ ... initial velocity along longitude direction
$v_2$ ... initial velocity along meridian
$v_3$ ... initial vertical (radial) velocity component
$az$ ... azimuth

$\Delta\phi$ ... difference in longitude
$\lambda$ ... latitude
$M$ ... molar mass
$R_{\mathrm{moon}}$ ... radius of body

A ballistic molecule moves on a plane that goes through the center of sphere/body; the ground track is thus part of a great circle.

## 4.2.1 Constant gravity

For constant $g$,

$$t = 2v_3/g \tag{4.1}$$

$$d = \frac{2}{g}v_3\sqrt{v_1^2 + v_2^2} \tag{4.2}$$

If $|v| > 0.4v_{\mathrm{esc}}$, then use non-uniform gravity formulae (Sec. 4.2.2)
If $|v| > v_{\mathrm{esc}}$, then gravitational escape
The landing latitude and longitude $(\lambda_2, \phi_1 + \Delta\phi)$ are calculated from the starting coordinates $(\lambda_1, \phi_1)$ with the following equations:

$$\cos(az) = v_2/\sqrt{v_1^2 + v_2^2} \tag{4.3}$$

$$\sin\lambda_2 = \sin(d/R_{\mathrm{moon}})\cos(\lambda_1)\cos(az) + \sin(\lambda_1)\cos(d/R_{\mathrm{moon}}) \tag{4.4}$$

$$\cos\lambda_2 = \sqrt{1 - \sin^2\lambda_2} \tag{4.5}$$

$$\cos(\Delta\phi) = \frac{\cos(d/R_{\mathrm{moon}})\cos(\lambda_1) - \sin(\lambda_1)\sin(d/R_{\mathrm{moon}})\cos(az)}{\cos\lambda_2} \tag{4.6}$$

Roundoff issues: if $\cos(\Delta\phi) > +1$ then $\cos(\Delta\phi) = +1$; if $\cos(\Delta\phi) < -1$ then $\cos(\Delta\phi) = -1$.

$p_r(2) = \arcsin(\sin\lambda_2)$
$\Delta\phi = \arccos(\cos(\Delta\phi))$ for normalization
if $v_1 < 0$, then $\Delta\phi = -\Delta\phi$
$p_r(1) = p_r(1) + \Delta\phi$
if $(\cos\lambda_2 == 0)$ then on pole
$p_r(1)$ is normalized to $0...360°$.

$p_t = p_t + t$

## 4.2.2 Non-uniform gravity

Ballistic travel distance $d$ and flight duration $t$ can also be calculated analytically for a radially dependent gravitational acceleration. Radial variations in $g$ are small for typical thermal speeds on Mercury and on the Moon, but necessary for Ceres and for super-thermal species on the Moon. The following equations are derived from those in Vogel (1966) and Kegerreis et al. (2017).

$a$ ... semi-major axis of ballistic trajectory
$e$ ... eccentricity of ballistic trajectory
$\alpha$ ... zenith angle of launch velocity, $\alpha = \arctan\left(\sqrt{v_1^2 + v_2^2}/v_3\right)$
Instead of (4.1) and (4.2) use

$$\gamma = (|v|/v_{\text{esc}})^2 \tag{4.7}$$

$$a = \frac{R_{\text{moon}}}{2(1-\gamma)} \tag{4.8}$$

$$e = \sqrt{1 - 4\gamma(1-\gamma)\sin^2\alpha} \tag{4.9}$$

$$d = 2R_{\text{moon}}\arccos\left(\frac{1}{e}(1 - 2\gamma\sin^2\alpha)\right) \tag{4.10}$$

$$E_p = 2\arctan\left(\sqrt{\frac{1+e}{1-e}}\tan\frac{d}{4R_{\text{moon}}}\right) \tag{4.11}$$

$$t = \frac{R_{\text{moon}}}{v_{\text{esc}}}\frac{E_p + e\sin E_p}{(1-\gamma)^{3/2}} \tag{4.12}$$

These equations are not suitable for small launch velocities due to roundoff.

Roundoff issues:

a) If $e$ is very close to 1 (fast near-horizontal launch), then based on Taylor expansion of (4.10) and (4.11),

$$d = 4\gamma R_{\text{moon}}\sin\alpha \tag{4.13}$$

$$E_p = 2\arctan\sqrt{\frac{\gamma}{1-\gamma}} \tag{4.14}$$

b) If $1 - 2\gamma\sin^2\alpha > e$ (horizontal launch), do something, otherwise $d = \texttt{NaN}$

Then use (4.3)–(4.6) as before.

## 4.2.3 Coriolis effect

The Coriolis effect is incorporated by adding tangential velocities but subtracting the distance the surface has traveled during time of flight.

At launch:
$$v_1 = v_1 - \frac{2\pi R_{\text{moon}}}{\text{siderealDay}}\cos(p_r(2)) \tag{4.15}$$

After landing:
$$p_r(1) = p_r(1) + t/\text{siderealDay} \tag{4.16}$$

The Coriolis effect is negligible on the Moon and on Mercury, but noticeable on Ceres.

| | $M$ | $\tau_{dissoc}$ (s) | |
|---|---|---|---|
| $H_2O$ | 18.015 | 20×3600 | Potter and del Duca (1964) |
| $H_2O$ | | 1/12.6e-6 | Crovisier (1989), normal sun |
| $H_2O$ | | 1/23.0e-6 | Crovisier (1989), active sun |
| He | 4.0026 | 1.9e7 | Killen and Ip (1999) |
| Ar-40 | 39.96 | 3.2e6 | Killen and Ip (1999) |

Table 4.1: Some pertinent parameters. $\tau_{dissoc}$ = photo-dissociation time scale at 1 AU for normal solar activity.

# 4.3 Other Model Components

## 4.3.1 Initial velocities

At launch, each of the three cartesian velocity components is picked from a probability distribution based on the surface temperature. Various probability distributions can be implemented, if desired.

For a Maxwellian distribution, each velocity component is picked from a Gaussian distribution with standard deviation $\sigma = \sqrt{T_{\mathrm{surf}} 8314.5/M}$. This also results in uniformly distributed launch azimuths.

A Maxwell-Boltzmann-Flux (also known as Armand) distribution is provided as an option in the code. A method to generate a Rayleigh-type probability distribution is given in (Devroye, 1986, p29). Starting with a random number $y$, uniformly distributed between 0 and 1, $v_3 = \sqrt{2}\,\sigma\sqrt{-\log(y)}$ results in a probability distribution $P(v_3) = (v_3/\sigma^2)\exp(-v_3^2/2\sigma^2)$. This is the velocity component normal to the surface, and the two horizontal components are still Gaussian distributions, whith the same value for $\sigma$.

## 4.3.2 Photo-destruction

Molecules are lost in-flight by photo-destruction (Table 4.1), at a rate of $t/(\tau_{\mathrm{dissoc}}R^2)$, where $R$ is the distance from the sun, often approximated by the semi-major axis. A comprehensive compilation of photo-destruction rates can be found in Huebner et al. (1992). A database is maintained at http://phidrates.space.swri.edu/. Note that photo-destruction rates vary during the solar cycle.

Molecules in-flight behind a planetary body are shielded from solar radiation. If hop heights and hop distances are small compared to the radius of the body, the incident flux $Q > 0$ can be used to determine whether the starting or landing position is on the dayside or the night side, which then serves as an approximate estimate for whether the molecule is exposed to solar radiation.

## 4.3.3 Event driver

Process events over the time step of the thermal model $\Delta t_T$, e.g., one hour

```
if (p_t > Δt_T) exit
case(p_s < 0) exit !  not alive
case(p_s==0) !  leaving
    hop once, update p_t
case(p_s==1) !  landing
    if (incoldtrap) then
        p_t = ∞
        cycle
    endif
    evaluate τ_res(T_surf)
    p_t = p_t + τ_res
```

After all events within $\Delta t_T$ are processed, subtract $\Delta t_T$ from all times: if (p_s >= 0) $p_t = p_t - \Delta t_T$. (Moving time zero helps avoid truncation errors after a long run.)

### 4.3.4   Residence times

Temperature also sets the residence time of water molecules on the surface, which is negligible on most of the lunar dayside and very long on most of the lunar nightside. Many older models used a binary choice, where molecules either immediately hop on the day side or reside indefinitely on the surface on the nightside. This model uses a molecular residence time that depends continuously on temperature instead of a threshold temperature.

The residence time of an adsorbed molecule depends on the surface temperature $T$ and on the adsorbate density $\theta$ (number of $H_2O$ molecules per area). The average residence time may be written as

$$\tau_{\text{res}} = \frac{\theta_m}{S(T, \theta)} \tag{4.17}$$

where $S$ is the desorption rate and $\theta_m = 10^{19}$ m$^{-2}$ is the areal number density of a $H_2O$ monolayer. A special case of this parametrization is $\tau_{\text{res}} = c\theta_m/S(T)$, where $S$ is the sublimation rate of pure ice. For pure ice $c = 1$, whereas the residence times are longer for adsorbed water, $c > 1$. For example, $c = 8.2$ is reasonable for sub-monolayer coverage on lunar grains (Schorghofer, 2022). The functional form of $S(T)$ is almost the same as using a vibrational frequency $\nu$ multiplied by a Boltzmann (Arrhenius) factor, and $\tau_{\text{res}} = \nu^{-1} \exp(E/k_B T)$, where $E$ is the binding energy, which may depend on $\theta$.

For non-condensible exospheric species (e.g., helium), $\tau_{\text{res}} = 0$.

The simplest choice is to assign a single deterministic value to $\tau_{\text{res}}$, given the temperature. Residence times can also be distributed probabilistically, and these times are here denoted by $t \equiv t_{\text{res}}$. It would be tempting to distribute $t$ exponentially, $P(t) = (1/\tau) \exp(-t/\tau)$. However, the desorption rate (the number of molecules leaving the surface per area and time) is given by the time average of $S = \theta/t$, and the time average of $1/t$ diverges. Therefore, it is not possible to choose a $\tau$ such that $1/\tau = \langle 1/t \rangle$. The angled brackets denote the average over the probability distribution, $\langle X \rangle = \int_0^\infty X(t)P(t)dt$.

It is physically reasonable to argue that $1/t$ should be distributed exponentially. A transformation in probability distributions according to $\tau e^{-\tau/t} |d(1/t)| = P(t)|dt|$ quickly

results in

$$P(t) = \frac{\tau}{t^2} e^{-\tau/t} \tag{4.18}$$

This distribution has the properties $\langle 1 \rangle = 1$ and $\langle 1/t \rangle = 1/\tau$. Such a distribution can be generated by the inversion method (Devroye, 1986). When $y$ is distributed uniformly between 0 and 1, then $t = -\tau/\log y$ is distributed according to (4.18).

It is computationally convenient to calculate or update the probability that a molecule leaves the surface during a time interval $\Delta t$, purely based on temperature. For a deterministic $\tau_{\mathrm{res}}$ this will be 0 or 1 depending on whether $\tau_{\mathrm{res}}$ is larger or smaller than $\Delta t$. For (4.18) this is going to be $\int_0^{\Delta t} P(t)\,dt = \exp(-\tau/\Delta t)$. Due to the extremely strong temperature dependence of desorption rates, the vast majority of molecules will have surface residence times either much shorter or much longer than any chosen $\Delta t$ interval for temperature updates. Only in a narrow range of temperatures will $\tau_{\mathrm{res}}$ be similar to $\Delta t$. For deterministically determined $\tau_{\mathrm{res}}$ this can lead to computational artifacts, such as a large number of molecules being released suddenly or getting stuck. Probabilistically distributed residence times mitigate this problem.

Discussion: A fraction of particles bounces elastically from the surface rather than accommodating thermally and leaving at a velocity unrelated to the incoming velocity. The fraction is closely related to the "accommodation coefficient" or "condensation coefficient", and it is temperature dependent. The equilibrium vapor pressure is defined as the flux of water molecules from the gas to the condensed phase being equal to the flux in the opposite direction. Elastic (non-condensing) bounces are not directly implemented in the model.

The exosphere model was used in Schorghofer (2014) (with constant $g$) and Schorghofer et al. (2016, 2017a,b) (with non-uniform gravity).

# Bibliography

Crovisier, J., 1989. The photodissociation of water in cometary atmospheres. *Astron. Astrophys.* 213:459–464.

Devroye, L., 1986. *Non-Uniform Random Variate Generation.* Springer. http://www.nrbook.com/devroye/.

Huebner, W. F., Keady, J. J., and Lyon, S. P., 1992. Solar photo rates for planetary atmospheres and atmospheric pollutants. *Astrophysics and Space Science* 195:1–294. doi: 10.1007/978-94-017-3023-5_1.

Kegerreis, J. A., Eke, V. R., Massey, R. J., Beaumont, S. K., Elphic, R. C., and Teodoro, L. F., 2017. Evidence for a localized source of the argon in the lunar exosphere. *J. Geophys. Res.* 122:2163–2181. doi: 10.1002/2017JE005352.

Killen, R. M. and Ip, W.-H., 1999. The surface-bounded atmospheres of Mercury and the Moon. *Reviews of Geophysics* 37:361–406. doi: 10.1029/1999RG900001.

Potter, A. E. and del Duca, B., 1964. Lifetime in space of possible parent molecules of cometary radicals. *Icarus* 3:103. doi: 10.1016/0019-1035(64)90051-X.

Schorghofer, N., 2014. Migration calculations for water in the exosphere of the Moon: Dusk-dawn asymmetry, heterogeneous trapping, and D/H fractionation. *Geophys. Res. Lett.* 41: 4888–4893. doi: 10.1002/2014GL060820.

Schorghofer, N., 2022. Gradual sequestration of water at lunar polar conditions due to temperature cycles. *Astrophys. J. Lett.* 927(2):L34. doi: 10.3847/2041-8213/ac5a48.

Schorghofer, N., Mazarico, E., Platz, T., Preusker, F., Schröder, S., Raymond, C., and Russell, C., 2016. The permanently shadowed regions of dwarf planet Ceres. *Geophys. Res. Lett.* 43:6783–6789. doi: 10.1002/2016GL069368.

Schorghofer, N., Byrne, S., Landis, M. E., Mazarico, E., Prettyman, T. H., Schmidt, B. E., Villarreal, M. N., Castillo-Rogez, J., Raymond, C. A., and Russell, C. T., 2017a. The putative cerean exosphere. *Astrophys. J.* 850:85. doi: 10.3847/1538-4357/aa932f.

Schorghofer, N., Lucey, P., and Williams, J.-P., 2017b. Theoretical time variability of mobile water on the moon and its geographic pattern. *Icarus* 298:111–116. doi: 10.1016/j.icarus.2017.01.029.

Vogel, U., 1966. Molecular fluxes in the lunar atmosphere. *Planetary and Space Science* 14: 1233–1252. doi: 10.1016/0032-0633(66)90078-X.